Origin and Evolution of Synoptic-Scale Vortices Initiated at Low Level Downwind of the Hoggar Mountains

Jean-Philippe Duvel

Origin and evolution of synoptic-scale vortices initiated at low-level downwind of the Hoggar Mountains

Jean-Philippe Duvel

Laboratoire de Météorologie Dynamique, CNRS, Paris, France

Submitted to Monthly Weather Review

December 2022

Revised version: March 2023

Corresponding author address:
Laboratoire de Météorologie Dynamique,
École Normale Supérieure,
24, rue Lhomond, F75231 Paris, France
jpduvel@lmd.ipsl.fr

ABSTRACT

Numerous low-level vortices are initiated downwind of the Hoggar Mountains and progress towards the Atlantic coast on the northern path of African Easterly Waves (AEWs). These vortices occur mostly in July and August and more specifically when the northern position of the Saharan heat low (SHL) generates stronger and vertically expanded easterly winds over Hoggar mountains. At synoptic time-scales, a composite analysis reveals that vortex initiation and westward motion are also statistically triggered by a reinforcement of these easterly winds by a wide and persistent high-pressure anomaly developing around the Strait of Gibraltar and by a weak wave trough approaching from the east. The vortices are generated in the lee of the Hoggar, about 1000 km west of this approaching trough, and intensify rapidly. The evolution of the vortex perturbation is afterward comparable with the known evolution of the AEWs of the northern path and suggest a growth due to dry barotropic and baroclinic processes induced in particular by the strong cyclonic shear between the reinforced easterly winds and the monsoon flow. These results show that vortex genesis promoted by changes in orographic forcing due to the strengthening of easterly winds over Hoggar mountains is a source of intensification of the northern path of AEWs in July and August. These results also provide a possible mechanism to explain the role of the SHL and of particular mid-latitude intraseasonal disturbances on the intensity of these waves.

1. Introduction

Over West Africa, synoptic-scale vortices associated with the trough of African Easterly Waves (AEWs) are moving on two paths located roughly on either side of 15°N. Vortices on the northern path are dry and located mostly at low-level (i.e. ~850hPa), while vortices on the southern path are associated with deep convection and located mostly at mid-level (i.e. ~700hPa) near the African Easterly Jet (AEJ) (see e.g., Thorncroft and Hodges 2001, Chen et al. 2008, Hopsch et al. 2007, Duvel 2021). The initiation of a vortex at a given pressure level corresponds to a deepening of the wave trough and therefore to an intensification of the AEW. This deepening will sometimes persist for long distances over West Africa and the Atlantic Ocean where vortices of both paths are known sources of tropical storms and hurricanes (see e.g., Hopsch et al. 2007, Chen et al. 2008, Chen and Liu 2014, Russel et al. 2017, Duvel 2021). In July and August, low-level vortices on the northern path are initiated mostly over a small region in the lee of Hoggar mountains Duvel (2021). The objective of this paper is to explore the conditions of formation of these “Hoggar vortices”, in relation to

seasonal and intraseasonal variations of the atmospheric circulation over the Hoggar orography.

The role of orography in triggering or intensifying AEW on the northern (hereafter AEW-N) or the southern (AEW-S) path has been proposed by many studies since pioneer work based on radiosonde measurements. Carlson (1969) first suggested that the origin of AEW-S could be linked to moist convection over the topography of central and eastern Africa. This role of orographic convection has been later established in more detail by several studies using meteorological analyzes and satellite measurements (Reed et al. 1988, Thorncroft and Hodges 2001, Berry and Thorncroft 2005, Mekonnen et al. 2006, Mekonnen and Rossow 2018). Dry orographic processes were also mentioned, like in Reed et al. (1988) who identified a cluster of AEW-N initiations located over the Sahara downwind of the Hoggar Mountains (~5°E, 24°N). Thorncroft and Hodges (2001) also found more frequent low-level vortex initiation downstream of the Hoggar Mountains and invoked the possible role of orography in the genesis of the low-level northern path disturbances. Duvel (2021) found that most of the low-level AEW-N vortices that reach the Atlantic Ocean, where they may trigger tropical cyclones, are initiated just west of the Hoggar Mountains in July and August. In addition to their potential role in cyclogenesis, Fiedler et al. (2014) found many of these low-level cyclonic disturbances are at the origin of Saharan dust lifting between the Hoggar and the Atlantic Ocean.

Studies based on numerical model simulations also suggested that the interaction between the Hoggar mountains and the large-scale flow could impact AEW-N. Thorncroft and Rowell (1998) showed that the strength of the low-level northeasterly flow over the Hoggar impact AEW-N amplitude. Hamilton et al. (2020) showed that the wave kinetic energy at low-level is reduced north of 15°N over West Africa when the topography is reduced or removed. White et al. (2021) showed more specifically a large reduction of the kinetic energy of AEW-N when the Hoggar and Tibesti Mountains are removed, due to reduction in baroclinic energy conversion related to reduced vertical wind shear. The initiation of vortices by a dry flow around a mountain was studied in Mozer and Zehnder (1996a, b) using an idealized numerical model. They showed that the blocking of an easterly flow by the Hoggar mountain may generate a barotropically unstable jet at low level which produces lee vortices downstream, being a possible source of AEW-N. Smaller meso-scale vortices are also initiated in the cyclonically sheared strip between the Harmattan and the monsoon flow. For

example, Bou Karam et al. (2009) studied short-lived and stationary vortices of smaller sizes initiated south of the Hoggar Mountains.

Previous studies have therefore suggested that the orographic forcing of the Hoggar plays a role in the initiation or intensification of AEW-N. In contrast with AEW-S, the deep convection must have little direct influence on wave initiation and growth for AEW-N path that is located north of 15°N over the Sahara Desert. Moreover, the AEW-N path is located more than 10° north of the AEJ core and near the surface, suggesting that physical sources other than AEJ instabilities may play a significant role on AEW-N activity. The literature review above shows that few papers have specifically addressed the observed seasonal and intraseasonal mechanisms behind the initiation of vortices downwind of the Hoggar and the impact of these vortices on AEW-N activity. These papers are based either on idealized simulations (Mozer and Zehnder, 1996b) or on sensitivity studies using numerical models with or without orography (see e.g., Hamilton et al. 2020, White et al. 2021). These sensitivity studies provide an estimate of the overall impact of orography on AEW-N, but as the removal of orography also significantly affects the mean dynamics and thermodynamics, it is difficult to isolate the specific orography processes that play a role in the AEW-N dynamics.

The objective of this paper is to study the origin of the observed initiation of low-level vortices in the lee of the Hoggar by relating this initiation to characteristics of the large-scale flow over this mountain. This paper considers two time-scales, the seasonal time scale to explore the average large-scale conditions that may explain why the Hoggar vortices are mostly initiated in July and August and the synoptic time scales that gives the particular conditions at time of vortex initiation. Section 2 presents the analysis approach and gives a statistic on the vortex tracks and on their impact on the AEW-N signal. The origin of the seasonal variation of the circulation over the Hoggar and its potential effect on vortex initiation and propagation is discussed in section 3. The conditions of formation of the vortices at synoptic time-scales (i.e. 2-10 days) are presented in section 4 and the characteristics of the vortices as they move toward the African coast are presented in section 5. The impact of these results on the origin of AEW-N is discussed in section 6.

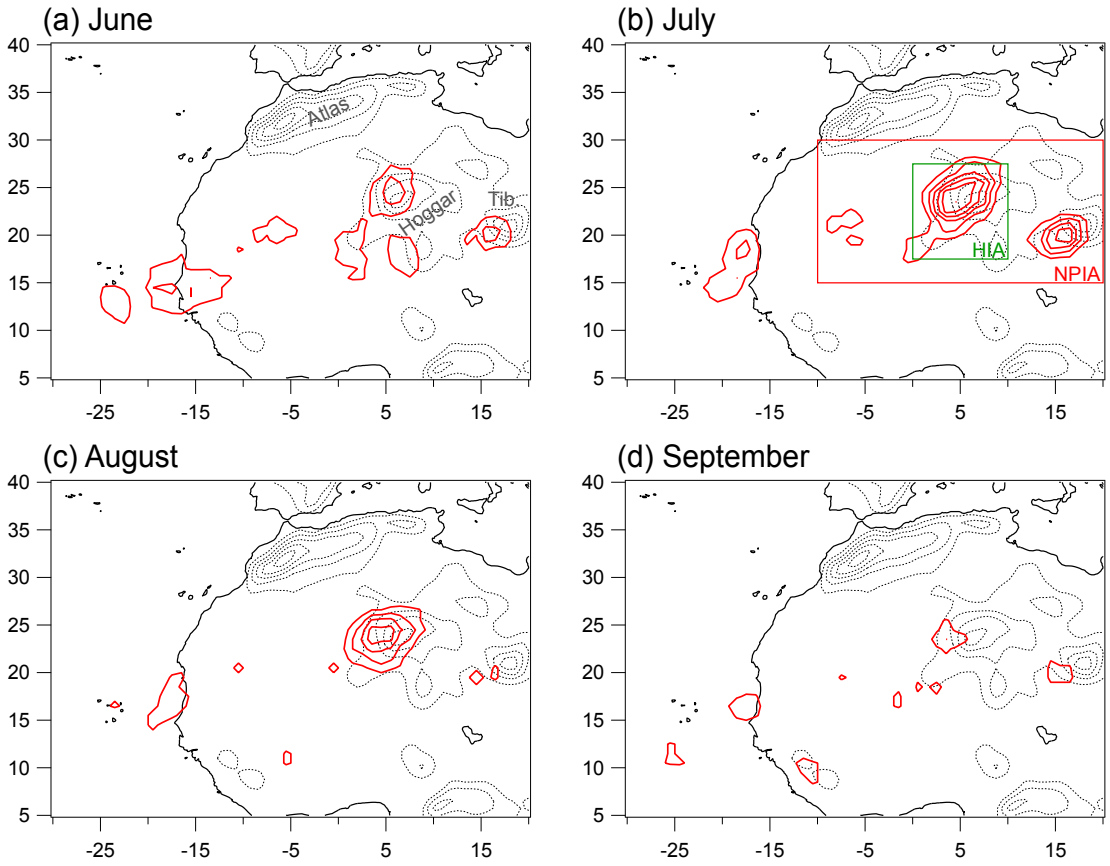

Figure 1: (**red contours**) Number of primary "Atlantic Vortex" initiations for a given month in 1° boxes for the 38 years. For a better legibility, initiation fields are smoothed by a 3°x3° running mean. The first contour is 0.5 and the contour increment is 0.5. (**black dotted contours**) Orography with a contours every 250m from 500m. On panel b, the red rectangle defines the North Path Initiation Area (NPIA) for initiation of AEW-N vortices, the green square defines the Hoggar Initiation Area (HIA) for "Hoggar vortices"

2. Analysis approaches and vortex statistics

Vortex tracking algorithm

The analysis is based on ERA-Interim (Dee et al. 2011) meteorological re-analyses between 1980 and 2017 with a horizontal resolution of 0.75° x 0.75° and a 6-hour time step. In order to assess the proper representation of the vortices in ERA-I and to analyze possible impact of these vortices on the cloudiness, we also use brightness temperatures of the CLAUS (Cloud Archive User Service) dataset (Hodges et al., 2000) that are available with a 3-hour time step for years 1983 to 2009. The set of vortex tracks used in this study is the same as that used in Duvel (2021) and is obtained using the objective tracking approach described in Duvel (2015) and Duvel et al. (2017). This approach is based on geopotential height anomaly $\Delta\phi$ for a particular isobar (850 hPa here for AEW-N vortices). At a given grid point, $\Delta\phi$ is defined as the difference between the geopotential height and its average

over a region of ±7.5° (i.e., ±10 ERA-I gridpoints) centered on the grid point. The "vortex area" is an ensemble of continuous model grid points with values of $\Delta\phi$ lower than a negative threshold. This threshold is adjusted for each vortex and each time step to limit the vortex size to a maximum area of 100 model grid points (i.e., a radius of 4.2° for a circular shape). The intensity of a vortex is given by the minimum value $\Delta\phi_{min}$ (i.e., maximum absolute value) of $\Delta\phi$ in the vortex area. A given vortex is tracked over time by considering the overlap between the vortex areas for two consecutive time steps. A vortex track is therefore a time series of the successive position of the barycenter (i.e. the center weighted by $\Delta\phi$) of these vortex areas, the first position being considered as the initiation location. As in Duvel (2021), we only consider vortex tracks that last more than two days and remain at least one day over the Atlantic Ocean. These vortices are called "Atlantic vortices" hereinafter. For the "Atlantic vortex" distribution maps reported in Figure 1, we consider only primary vortex initiations at 850 hPa. A primary initiation corresponds to a first vortex detection that does not result from the vertical extension on an already existing vortex track at another pressure level (700 hPa here). This distinction is mostly useful for the AEW-S path and near the coast where many low-level initiations are related to downward extension of mid-level vortices (Duvel 2021). The area of initiation of AEW-N vortices is defined as the area north of 15°N and east of 10°W, which is the Northern Path Initiation Area (NPIA) outlined in red in Figure 1b. Over the NPIA, most low-level AEW-N vortices initiations are primary initiations (Duvel, 2021) and this distinction is therefore not made in what follows. A vortex track is considered cyclogenetic if it is located within 3° of an IBTrACS system (Knapp et al. 2010) for at least one time step.

Atlantic Vortex initiation statistics

Between June and September, there are about 3 Atlantic vortices initiated each month at 850 hPa over the NPIA and about 12% of these vortices are cyclogenetic (Table 1). There is also a large seasonal variation of the number of initiations, with a maximum of 4.4 per month in July and less than 2 per month in September. The cyclogenetic efficiency of these vortices (i.e., the probability that their track matches an IBTrACS system) has a sharp maximum of 29% in August. As discussed in Duvel (2021) the cyclogenesis efficiency of these dry AEW-N vortices is indeed as large as the AEW-S vortices in August when the cyclogenesis potential index of the Atlantic Ocean is a maximum. The cyclogenesis efficiency of AEW-N vortices is small on the average because they peak in July when this index is smaller.

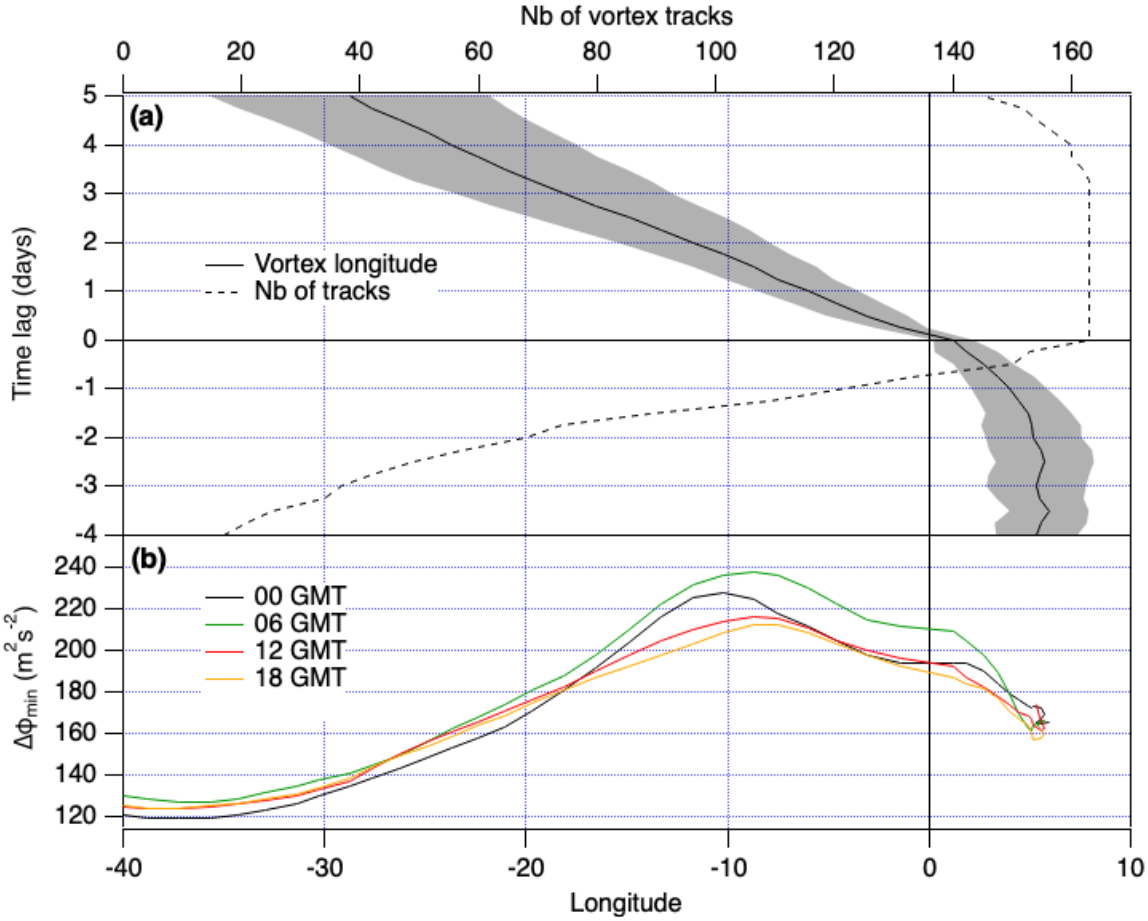

Figure 2: (a) Average (solid) and standard deviation (gray part) of the Hoggar vortex longitude (bottom axis) as a function of the time lag in regard to the crossing of the Greenwich meridian for vortex initiated in the main development region (0°E to 10°E; 17.5°N to 27.5°N) in July and August; (dashed) Number of vortex tracks (top axis) considered for the different time lags. (b) Corresponding longitudinal distribution of the average absolute value of $\Delta\phi_{min}$ for four hours of the day.

This paper focuses on Atlantic vortices initiated in the Hoggar Initiation Area (HIA: 0°E to 10°E; 17.5°N to 27.5°N; green square in Fig. 1b). These vortices are hereafter called "Hoggar vortices". For the 38 years, there are 166 Hoggar vortices that represent more than 60% of the Atlantic vortices of the AEW-N path in July and August. These Hoggar vortices have a cyclogenetic efficiency comparable to that of all Atlantic Vortices of the AEW-N path (Table 1).

	(NPIA) North Path Vortices		(HIA) Hoggar Vortices	
	Nb. Initiations	Cyclogenetic	Nb. Initiations	Cyclogenetic
June	2.7	1%	1.2	2%
July	**4.4**	5%	**2.4**	2%
August	3.4	**29%**	1.9	**29%**
September	1.9	15%	0.6	13%
Average	3.1	12%	1.5	12%

Table 1: Monthly average number of initiations (over 1980-2017) and average cyclogenetic probability of Atlantic vortices of the north path initiated in the NPIA and in the HIA. Seasonal maxima are highlighted in bold.

Figure 2 represents the average longitude and strength attained by the Hoggar vortices at different time lags after they cross the Greenwich meridian. Hoggar vortices move westward with an average speed of about 7.5 ms^{-1}. The beginning of their westward progression is associated with a strengthening of the vortex, as revealed by the increasing absolute value of $\Delta\phi_{min}$ before the passage on the Greenwich meridian (Fig.2b). Before that, due to the persistent depression in the lee of the Hoggar, many vortices first detected by the tracking algorithm in the HIA remain motionless and weak for a variable number of days (Fig.2a). In the following, only diurnal averages will be considered, but it is worth noting that there is a diurnal variation of the dynamic and thermodynamic structure of the boundary layer over West Africa (Parker et al. 2005, Abdou et al. 2010). This is due to the weak turbulent mixing in the boundary layer during nighttime that decreases the effect of the surface friction and generates a low-level vertical stratification. This favors the development of nighttime low-level jets that are maximal at sunrise and that may impact Hoggar vortex intensity. This diurnal cycle has indeed a consistent signature on the vortex intensity over continental regions with maximum absolute value of $\Delta\phi_{min}$ at 0600 GMT and minimum at 1800 GMT (Fig.2b).

Atlantic Vortex Occurrence and AEW-N amplitude

The AEW-N vortex occurrence, i.e. the number of hours during which a vortex barycenter is present in a given area, is reported in Figure 3. These maps reveal the most probable trajectory of the low-level Atlantic vortices of the north path and show the predominance of vortices initiated near the Hoggar and the Tibesti in July and August. These vortices propagate southwestward to the Atlantic Ocean roughly along the cyclonically sheared strip between the Harmattan wind and the monsoon flow. The relation between Atlantic Vortices and the AEW-N is studied by comparing the vortex occurrence to the AEW-N activity. This activity may be estimated by computing the perturbation kinetic energy K' (in J kg^{-1}) of the horizontal wind at low-level (see e.g., Rydbeck and Maloney 2014, Hamilton et al. 2020, White et al. 2021):

$$K' = \frac{1}{2}(u'^2 + v'^2) \qquad (1)$$

where u' and v' are the 2-10-day band-filtered zonal and meridional winds at 850hPa. The distribution of K' shows that regions of high AEW amplitude are also region of large vortex occurrence (Fig.3). In addition, the seasonal variation of K' is also in phase with that of the

vortex occurrence with maximum values in July. The maximum value of K' in July and August (Fig.3b and 3c) is obtained around 10°W, that is consistent with the longitude of maximum vortex intensity reported in figure 2b. Over the Atlantic, the decrease in K' despite the large vortex occurrence is due to the regular weakening of the average vortex amplitude as they move westward over the Atlantic (Fig.2b).

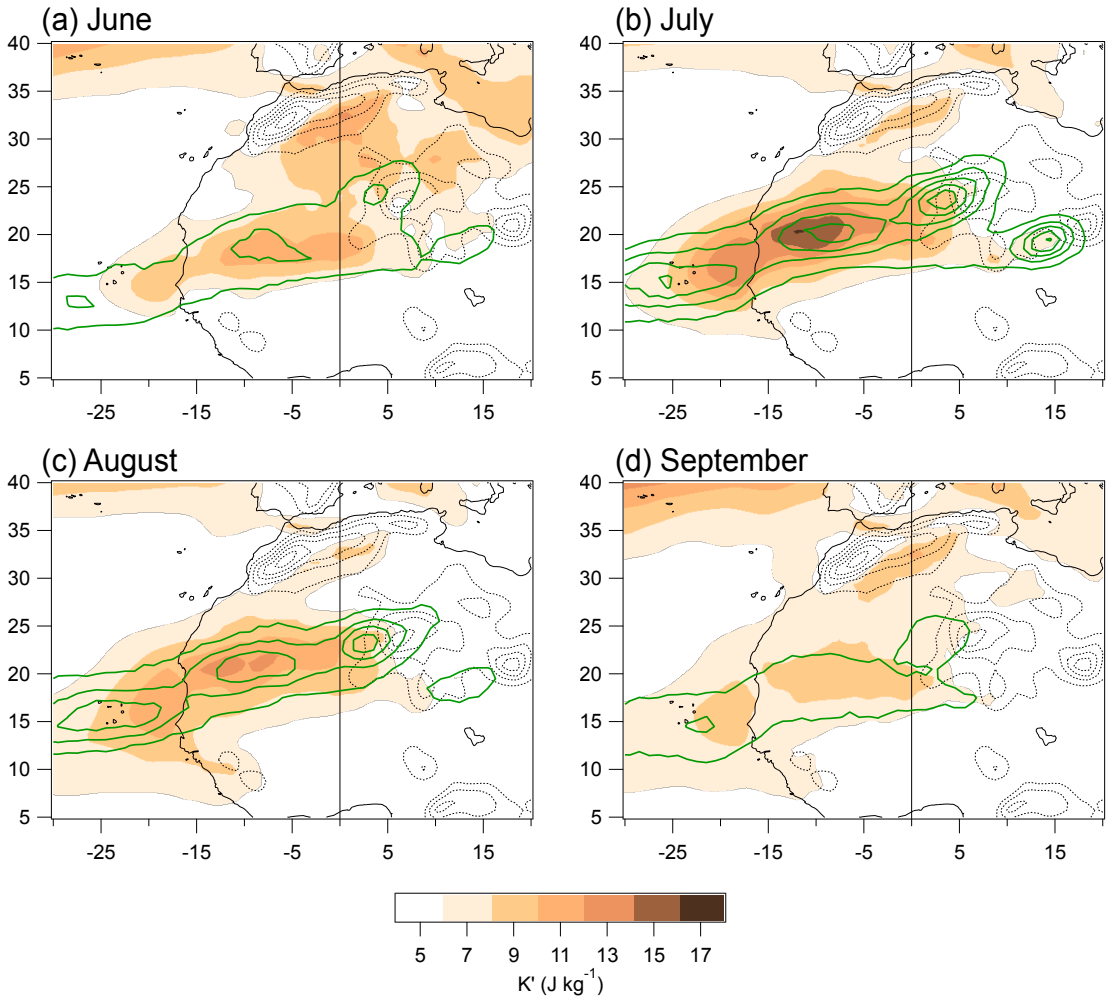

Figure 3: (**green contours**) Occurrence of AEW-N vortices initiated over the NPIA, expressed as the number of hours by month a vortex barycenter is present in a 1° box. For a better legibility, occurrence fields are smoothed by a 3°x3° running mean. The first contour is 0.5 and the contour increment is 1. (**colors**) Monthly average of the perturbation kinetic energy K' (Eq.1) (J kg^{-1}) of the horizontal wind at 850 hPa in the 2–10-day band. (**dotted black contours**) Orography with a contours every 250m from 500m.

The specific role of the Hoggar vortices on the AEW-N activity is estimated by comparing K' for periods with (HV) and without (No HV) active Hoggar vortices. Active Hoggar vortex periods are defined as all time-steps between d_0-1 day and d_0+4 days, d_0 being the ensemble of days at which each of the 166 Hoggar vortices crosses the Greenwich meridian. Active Hoggar vortex periods represent about 1/3 of the time for July and August. As for the average K', the distribution of K'(HV) for these active periods well corresponds to

the specific Hoggar vortex occurrence in July and August (Fig.4a). Compared to K'(No HV), K'(HV) is augmented by about 20% over the most active region around 20°N and 10°W (Fig.4b). This confirms that active Hoggar vortex periods correspond to enhanced AEW-N activity over West Africa. In contrast, K'(HV) is slightly reduced between Hoggar and Atlas Mountains around 27.5°N, possibly due to the relation between Hoggar vortex initiations and relatively stable (and thus giving smaller K') northeasterly winds associated with intraseasonal mid-latitudes perturbations (see section 4). Note that adding vortices initiated downwind of the Tibesti mountains (those around 20°N-15°E in Fig.1b), about 220 vortices cross the Greenwich meridian and K'(HV) is reinforced by about 30% around 20°N and 10°W compared to K'(No HV) (not shown). This highlights the fact that the impact of vortices initiated near the orography on the AEW amplitude is broader than the impact of the Hoggar vortices alone. Nevertheless, as the conditions of vortex initiation over the Tibesti and the Hoggar are slightly different, the following analyses will focus on Hoggar vortices only.

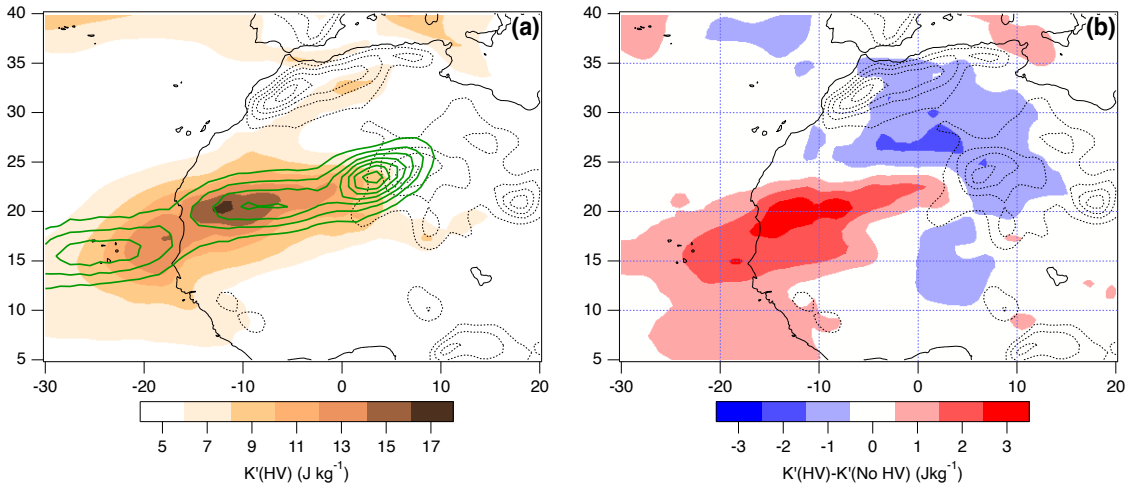

Figure 4: (a) (**colors**) Average perturbation kinetic energy K' (J kg^{-1}) of the horizontal wind at 850 hPa in the 2-10-day band in July and August for periods with active Hoggar vortices. (**green contours**) Occurrence of "Hoggar Vortices" initiated in the HIA, expressed as the number of hours a vortex barycenter is present in a 1° box. For a better legibility, occurrence fields are smoothed by a 3°x3° running mean. The first contour is 1 and the contour increment is 1. (b) (**colors**) Average K' difference between periods with (HV) and without (No HV) Hoggar vortices. All differences in red or blue are significant at more than 99%. (**dotted black contours**) Orography with a contours every 250m from 500m.

Composite analysis

In section 4, synoptic time-scale perturbations corresponding to Hoggar vortex initiation are studied using a composite analysis. The reference days d_0 of the composite are days when the barycenter of a Hoggar vortex crosses the Greenwich meridian. This meridian is the western boundary of the HIA and is crossed by Hoggar vortices while they strengthen and

begin their progression toward the coast (Fig. 2). This is therefore the relevant criteria to define the reference day d_0 of the Hoggar vortex composites. Composite fields are computed by averaging anomalies over the ensemble of days d_0. Anomalies of a given ERA-I field for each d_0 is computed as a difference between the daily mean field (4 timesteps beginning at 0 GMT) and a climatological value for this day of the year. This daily climatological value is obtained by linear interpolation between two monthly averages attributed to the 15th day of each month. The evolution of the average atmospheric state prior and after Hoggar vortex initiations is computed following the same procedure between d_0-4 days and d_0+4 days.

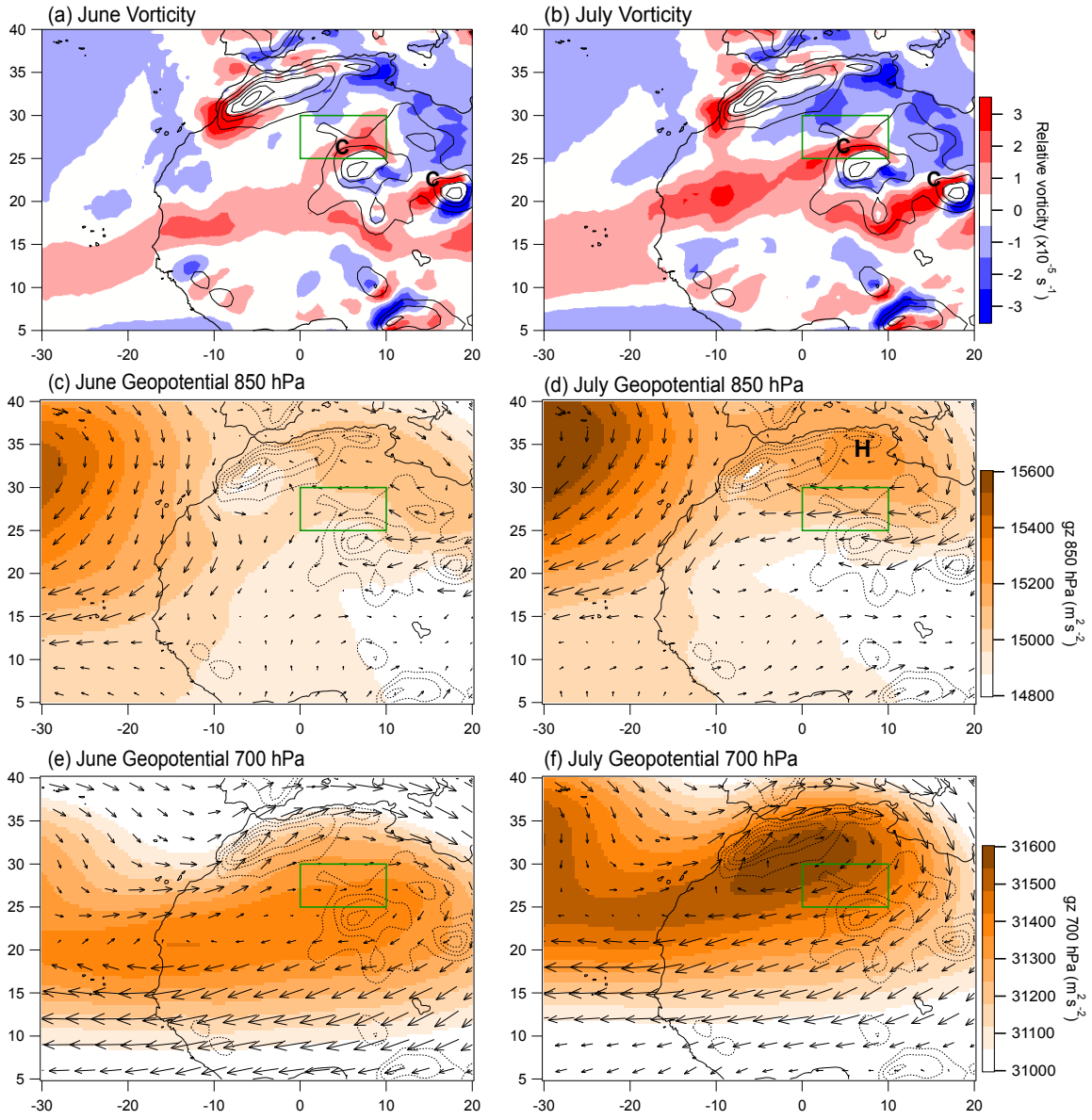

Figure 5: Average fields for June and July for: (a and b) Average relative vorticity at 900 hPa; (c and d) Average geopotential height and wind at 850hPa; arrows length is 4° for a wind of 10ms^{-1}; and (e and f) idem at 700 hPa. (black dotted contours) Orography with a contours every 250m from 500m. The region used in Figure 6 is highlighted in green.

3. Seasonal evolution of the large-scale environment

The objective of this section is to extract specificities of the large-scale circulation in July and August and to understand how they can favor vortex initiation in the lee side of the Hoggar mountains. As shown by Sultan and Janicot (2003), there is a sudden onset of the monsoon at the end of June due to the migration of Saharan Heat Low (SHL) and to different positive feedbacks partly linked to orography (Semazzi and Sun 1997). The resulting difference between June and July in low-level wind and vorticity (Fig. 5) reveals two important features that potentially have a significant impact on the increased frequency of Hoggar vortices in July. The first feature is the cyclonic vorticity north of Hoggar and Tibesti mountains (points C in Fig.5) which may be attributed to increased drag closer to the mountain that generates a cyclonic shear in the flow having the mountain to its left. This cyclonic vorticity is larger and extends further west in July. The second feature is the cyclonic strip between the Hoggar and the Atlantic coast due to the horizontal shear between the Harmattan and the monsoon flow. This cyclonic strip is stronger and displaced northward in July in good agreement with the AEW-N activity and vortex occurrence (Fig.3a and 3b). Note that part of the increase in mean vorticity, particularly near 10°W-20°N, must be due to the higher frequency of the vortex itself, but the increase in cyclonic shear is also due to the strengthening of the Harmattan and of the monsoon flow. These two points lead to a continuous and reinforced cyclonic strip between the leeward side of the Hoggar and the coast in July.

The development of this strong and continuous cyclonic strip in July is mostly due to the reinforcement of the low-level easterly circulation north of 20°N in association with the reinforced latitudinal pressure gradient at low-level (Fig.5c and 5d). Note that the reinforcement of the anticyclonic circulation of the Libyan High (Point H in Fig.5d) may be favored by orographic effect due to the northeastern edge of Atlas Mountains (Fig.5b). At higher levels, the high pressure generated mostly by the presence of the SHL is centered on the Hoggar in June, giving westerly winds to the northern side of the Hoggar, and reinforced and centered south of the Atlas in July, giving strong easterly winds to the northern side of the Hoggar (Fig.5e and 5f). The seasonal evolution of the zonal wind profiles north of the

Hoggar (0°E-10°E; 25°N-30°N; green rectangle in Figure 5) between May and October shows a clear reinforcement and a vertical extension of easterly winds from the surface up to

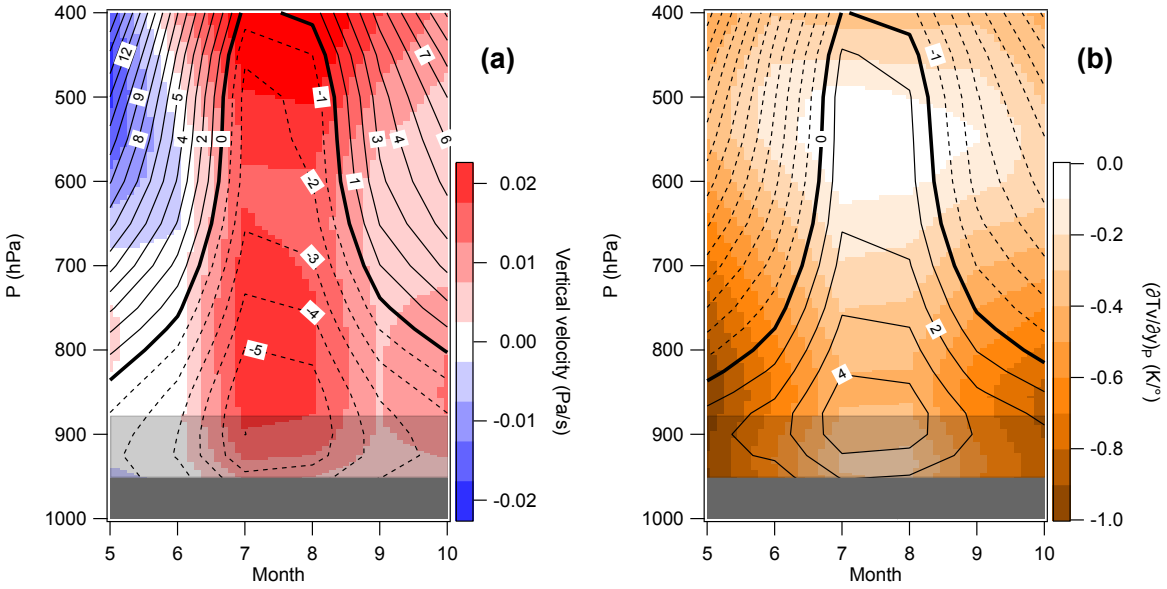

Figure 6: Evolution of monthly mean profiles for the region (0°E to 10°E; 25°N to 30°N; green region in Figure 5) between May and October for: (a) the zonal wind (contours, ms^{-1}) and vertical motion (colors in Pa s^{-1}, positive values for downward motion); (b) latitudinal gradient of the geopotential height (contours, m/°) and latitudinal gradient of the virtual temperature (colors in K/°). Maximum and average orography for the region is shown in light and dark grey respectively.

400 hPa in July and August, associated with reinforced subsidence (Fig.6a). This can be mostly attributed to the northward migration of the SHL that places the area north of the Hoggar under the southeastern descending branch of the Libyan High. Figure 6b shows that this can be also understood in term of local thermal wind structure for which the zonal geostrophic wind U_g on an isobar P_n is given by:

$$U_g(P_n) = -\frac{1}{f}\left(\frac{\partial \Phi(P_0)}{\partial y}\right)_P - \frac{R}{f}\sum_{i=1}^{n}\left(\frac{\partial \overline{T_{vi}}}{\partial y}\right)_P Ln(P_{i-1}/P_i) \qquad (2)$$

where f is the Coriolis parameter, $\phi(P_n)$ the geopotential height of the isobar P_n, $\overline{T_{vi}}$ is the average virtual temperature between the two pressure levels P_i and P_{i-1}, and R the gas constant for dry air. Figure 6b is computed using monthly means T_v and $\phi(P_0)$ taken in ERA-I. The stronger easterly wind near the surface in July is due to larger low-level latitudinal pressure gradient (first RHS term of Eq.2; contours in Fig.6b) between the Hoggar and the Mediterranean Sea (Fig.5c and d) that mostly results from the northward migration of the SHL, as described in Sultan and Janicot (2003). Second, this northward migration of the SHL reduces the magnitude of the latitudinal gradient of the virtual temperature (second RHS term of Eq.2; colors in Fig.6b) in July and August and maintains these easterlies up to 400 hPa.

Before July and after August, when the SHL is shifted southward, the larger absolute value of this gradient causes the easterlies to weaken and turn west rapidly with height.

In summary, this section shows that the stronger easterly winds over the Hoggar in July reinforce cyclonic vorticity north and west of the orography and could be at the origin of more frequent Hoggar vortex initiation during these months. In addition, the northward displacement and the strengthening of the cyclonic strip between the Hoggar and the coast in July may promote the development and maintenance of the vortex disturbance through barotropic and baroclinic processes, as shown by previous analyses of the energy source of AEW-N (see e.g., Norquist et al. 1977, Diedhiou et al. 2002, and section 5).

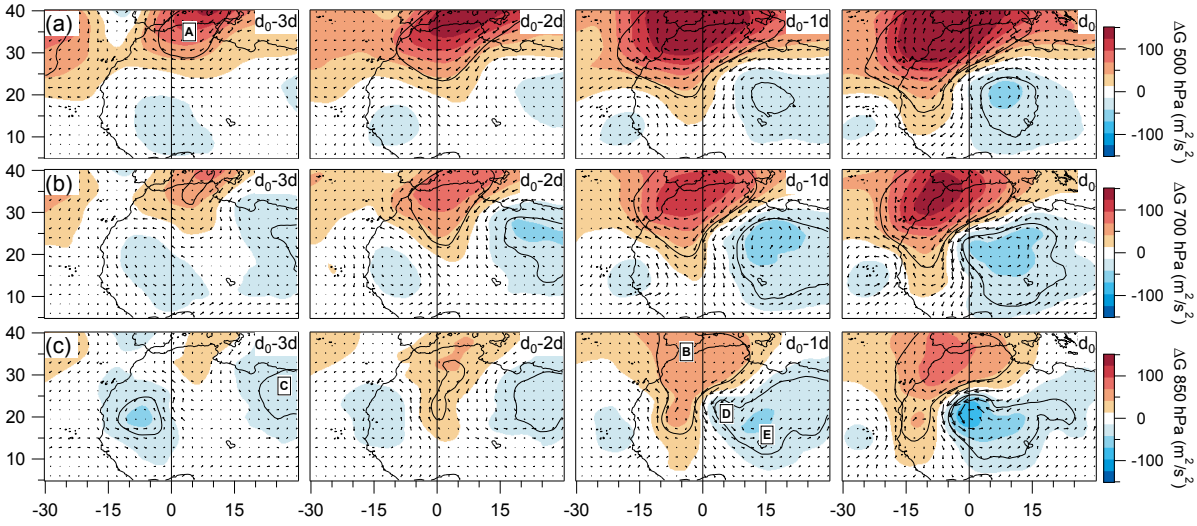

Figure 7: Composite of the horizontal wind anomaly (arrows, length of 5° for 5ms^{-1}) and of the geopotential height anomaly at (a) 500 hPa, (b) 700 hPa and (c) 850 hPa for the period [d_0 - 3 days, d_0]. The day d_0 is the day when the barycenter of the Hoggar vortex at 850 hPa crosses the Greenwich meridian. The black contour delineates regions for which the composite geopotential perturbation is significant at the 99% level.

4. Hoggar vortex genesis

The objective of this section is to determine large-scale and local conditions leading to Hoggar vortex initiations. To this end, composites of the 166 Hoggar vortices are computed for the dates of initiation d_0 and for each of the three days before and after d_0 (see section 2). Three days before Hoggar vortex initiation, there is a high-pressure anomaly significant at the 99% level above 700 hPa over a region centered near the Strait of Gibraltar (point A in Fig.7a). This anomaly amplifies, extends downward and spread horizontally, giving northeasterly winds blowing at 850 hPa over the Hoggar one day before d_0. A weak but statistically significant depression anomaly is also initiated at low-levels three days before d_0 near the Mediterranean Sea around 30°N and 30°E (point C in Fig.7c). The following days, this "easterly low" moves westward, extends up to 500 hPa, strengthens and contributes to

increase the northeasterly flow over the Hoggar. At d_0-1d, a secondary minimum in the 850 hPa geopotential height anomaly appears in the lee side of the Hoggar (point D in Fig.7c) more than 1000 km west of the "easterly low" which is still centered at 20°N-15°W and shifted southward compared to previous days (point E in Fig.7c). The secondary minimum may be considered as the initiation of the Hoggar vortex which then strongly intensifies between d_0-1d and d_0 in association with a horizontal expansion and a strengthening of the "Gibraltar high". At d_0, the vortex is centered on the Greenwich meridian and therefore at 10° west of the "easterly low" at 500hPa which continues its slow westward progression.

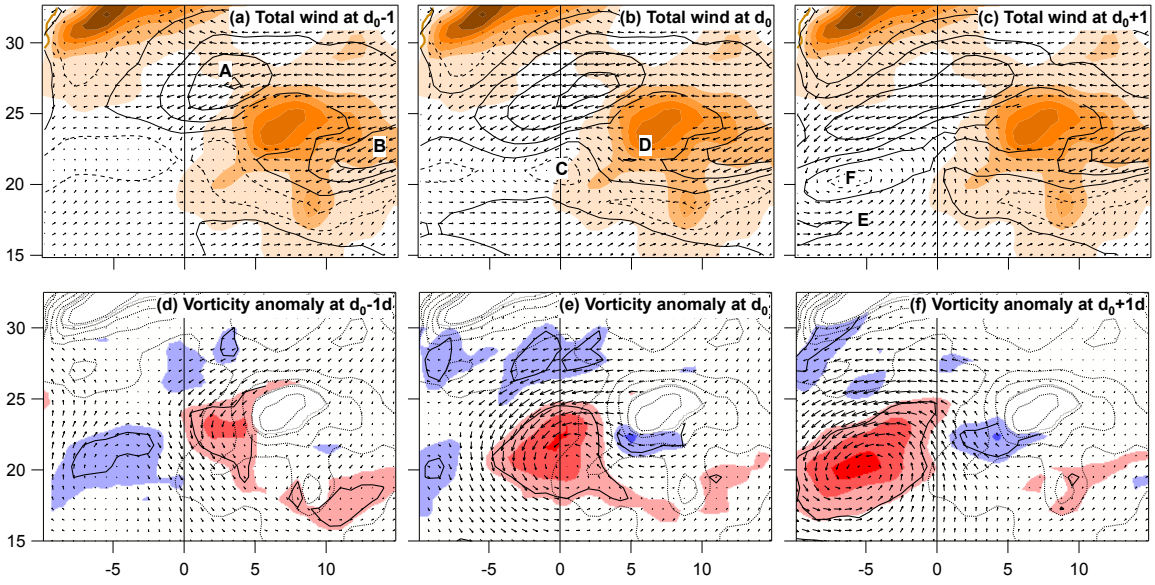

Figure 8: (a, b, c) Composite of the total wind field at 900 hPa at d_0-1 day, d_0, and d_0+1 day. Arrows length is 1° for 10ms^{-1} and black contours are the wind strength (dotted line for 2ms^{-1} and increment of 2ms^{-1}). (d, e, f) Composites of relative vorticity (colors as for Fig.5, black contour for statistical significance at 99%) and wind (arrows length is 1° for 5ms^{-1}) anomalies at 900 hPa. The orography with a height step of 200m is represented by colors for a, b and c and by dotted contours for d, e, and f.

Figure 8 highlights the low-level wind and vorticity evolution near the Hoggar at higher spatial resolution during vortex initiation. The wind speed is stronger northwest of the Hoggar, over the Tademaït Plateau (point A in Fig.8a), and between the Hoggar and the Tibesti (point B). However, only the wind west of the Hoggar is perturbed during these 3 days, showing the preponderance of dynamical processes downwind of the Hoggar on vortex initiation. One day before initiation, a significant relative vorticity anomaly extends the average vorticity strip (Fig.5b) in the lee of the Hoggar (Fig.8d). The vortex is then asymmetric with maximum vorticity and wind anomalies north of the vortex center (point C in Fig.8b). The northeast side of the vortex is alimented by an easterly flow deviated around the southern edge of the Hoggar mountain (point D). The next day, the center of the vortex

(point F in Fig. 8c) is located about 6° further west, giving a speed of about 7.7 ms^{-1} that corresponds to the north-east wind speed to its north. The southwesterly monsoon flow (point E in Fig.8c) is reinforced and recurves to form the eastern side of the vortex which is then more axisymmetric.

The dynamical perturbation due to the mountain is complex and involves different processes that may lead to the formation of vortices downwind. As discussed in Mozer and Zhender (1996a and b) (hereinafter MZa and MZb), the conservation of the potential vorticity for a dry flow passing south of an isolated mountain (without column depth change) may result in a low-level jet that is barotropically unstable, leading to the production of synoptic vortices that separate from the mountains and move downstream. However, the jet south of the Hoggar (point D) is weak here and the Hoggar vortex initiation seems more in agreement with the vortex generated during the transient period at the beginning of the MZ simulations. This transient period is associated with the formation of a so-called starting vortex attributed to column stretching as the air initially at the top of the mountain is forced downstream (Huppert and Brian 1976). In MZ simulations, the transient period results from the instantaneous incorporation of orography in the flow, but it could result here from the rapid intensification of the easterly flow over the mountain. A starting vortex indeed also appears for wind modulations due to planetary Rossby waves in an easterly flow over orography (Zehnder 1991). The evolution shown in figures 7 and 8 resembles the Zehnder results with a cyclonic vortex forming in the lee of the mountain while a wave trough is still quite far to the east, displaced southward (as point E in Fig.7c) and reinforced because of the conservation of the total vorticity. The fact that the vortex appears while the easterly flow is reinforced by the "Gibraltar high" and the approaching trough suggests that Hoggar vortex initiation process could be understood more as a starting vortex rather than a vortex due to barotropic instability of the jet south of the Hoggar. Nevertheless, such barotropic and baroclinic instabilities due to the strong cyclonic shear existing between the Greenwich meridian and the coast certainly plays a role in intensifying and maintaining the vortex, this is analyzed in the next section.

5. Hoggar vortex evolution

After its initiation, the vortex moves westward along 20°N and reaches a maximum strength around 10°W. The "Gibraltar high" remains quite stationary between d_0-1d and d_0+3d and provides strong easterly winds on the north side of the vortex during its genesis

and during its progression toward the coast (Fig.9a and 9b). Between d_0-1d and d_0+1d, these easterly winds are associated with a significant subsidence anomaly (Fig.9c) above the Hoggar associated with warm (Fig.9d) and dry (Fig.9a) anomalies in the vortex. These dry processes during the vortex genesis are consistent with the band of positive T_b anomaly measured from space east of the Greenwich meridian at d_0-1d (Fig. 9f) and associated with a northerly wind anomaly. The positive T_b anomaly is large and significant near 25°N at d_0 and consistent with subsiding warm and dry air north and west of the vortex center. During the vortex progression over the continent, warm and dry Saharan air is advected southward in the west side of the vortex. The resulting warm anomaly near the center of the vortex (Fig. 9d) gives a low-level warm-core structure that decreases the vortex cyclonic circulation above and confines the vortex circulation at low-levels.

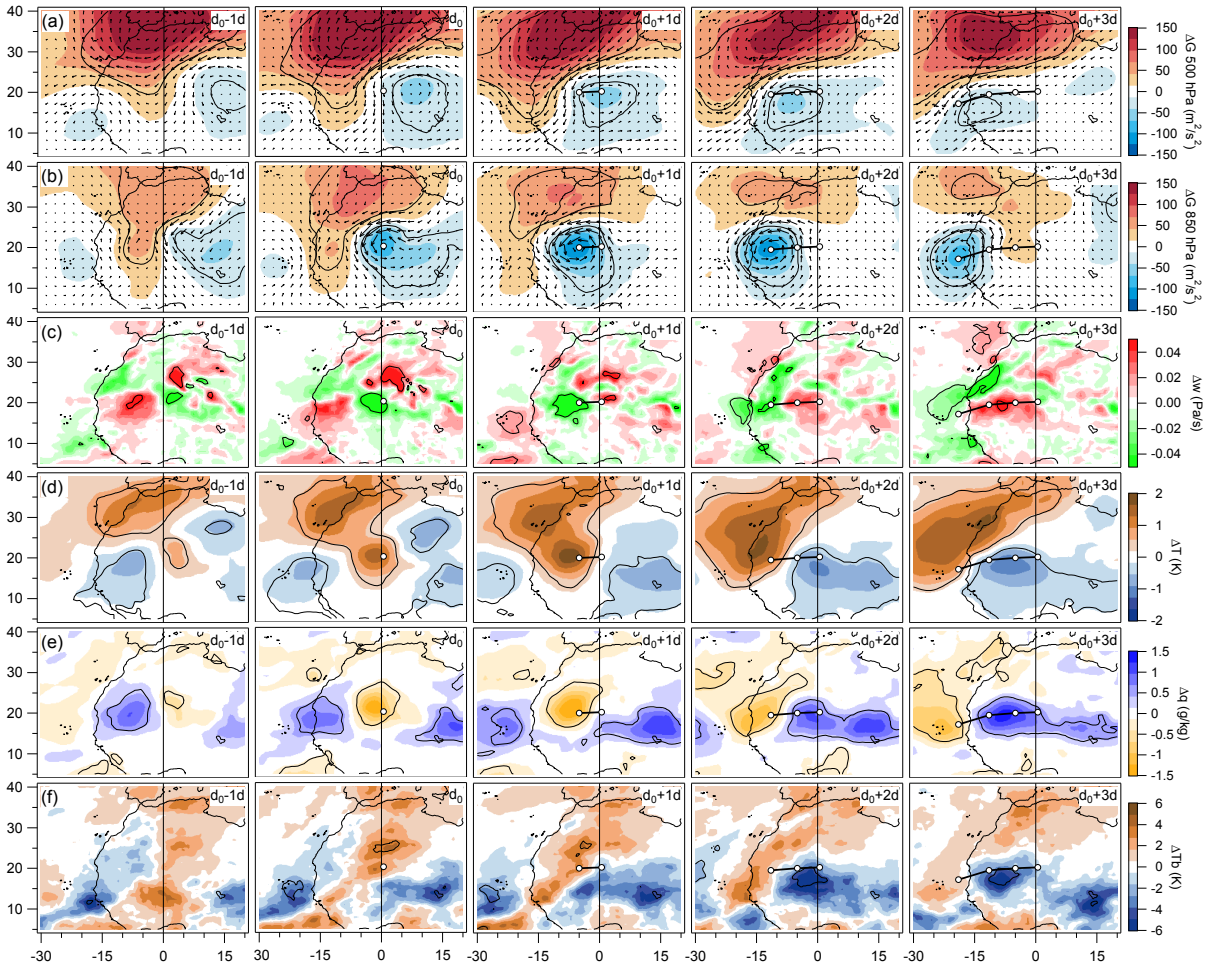

Figure 9: As in figure 7, but for the period [d_0-1, d_0 + 3 days] for the anomaly of different dynamical and thermodynamical parameters from top to bottom: (a) geopotential height ΔG at 500hPa and (b) 850 hPa, (c) vertical velocity Δω (positive downward), (d) temperature ΔT and (e) specific humidity Δq at 850 hPa, and (f) infrared window brightness temperature ΔT_b measured by the geosynchronous satellite Meteosat. The white markers represent the evolution of the position of the dynamical center of the 850 hPa vortex from d_0.

On the other hand, the warm anomaly over the Atlantic Ocean West of Morocco tends to maintain the anticyclonic geostrophic circulation around the "Gibraltar high" at 500 hPa (Fig. 9a). When the vortex reaches the coast, there is a large band of warm and dry anomaly over the ocean and a band of cold and moist anomaly over the Sahelian zone between 15°N and 20°N. This evolution of the low-level temperature and humidity (Fig. 9d and 9e) is consistent with the evolution of the observed anomaly of infrared brightness temperature (Fig. 9f). In particular, negative T_b anomalies, which correspond to enhanced mid and high cloud cover computed using thresholds at 230K and 210K (not shown) are associated with colder and moister air temperature at low-levels, especially at d_0+2d and d_0+3d. At this time, the high cloud cover north of 15°N is maximal in the east side of the vortex that is equivalent to the southerly wind sector of an AEW-N. This is in agreement with previous studies (see e.g., Duvel 1990, Gu et al. 2004, Kiladis et al. 2006) showing maximum convection in the southerly wind sector of the wave north of 15°N. This is in contrast with the maximum convection and mesoscale convective systems found in the wave trough around 10°N for AEW-S between the Greenwich meridian and the coast (see e.g., Kiladis et al. 2006, Núñez Ocasio et al. 2020). This moist anomaly over Sahelian regions is probably similar to the moisture surges discussed in detail in Couvreux et al. (2009) for June 2006 and to the northward burst of the West African monsoon studied in Cuesta et al. (2009) for the end of July 2006. On the opposite, the west side of the vortex with positive T_b anomalies indicates a region of suppressed convection ahead of the vortex due to dry and warm northerlies. As stated in section 2, some of these dry vortices can lead to cyclogenesis, either near the coast or later over the Atlantic (e.g. Chen et al. 2008, Chen and Liu 2014, Duvel 2021). They are however poorly cyclogenetic compared with vortices of the AEW-S partly because they tend to occur before the heart of the hurricane season, but also, as stated by Hopsch et al. (2010), because warm and dry conditions west of the AEW trough, caused by advection of Saharan air, inhibit the development of deep convection and further deepening of the wave trough.

Figure 10 shows the evolution of the anomalies of the three-dimensional dynamical structure of the vortex as it moves toward the coast. At d_0, the vortex is strongly asymmetric with an easterly wind anomaly of 4 ms^{-1} at 25°N and a westerly wind anomaly of only 1.5 m s^{-1} at 17°N (Fig.11a). The southerly wind perturbation on its east side is weak and vanishes above 800 hPa. This strong asymmetry of the wind anomaly is consistent with the transient period discussed above and suggests that the main driving force of the vortex formation at this early stage is the acceleration of the northeasterlies near the surface

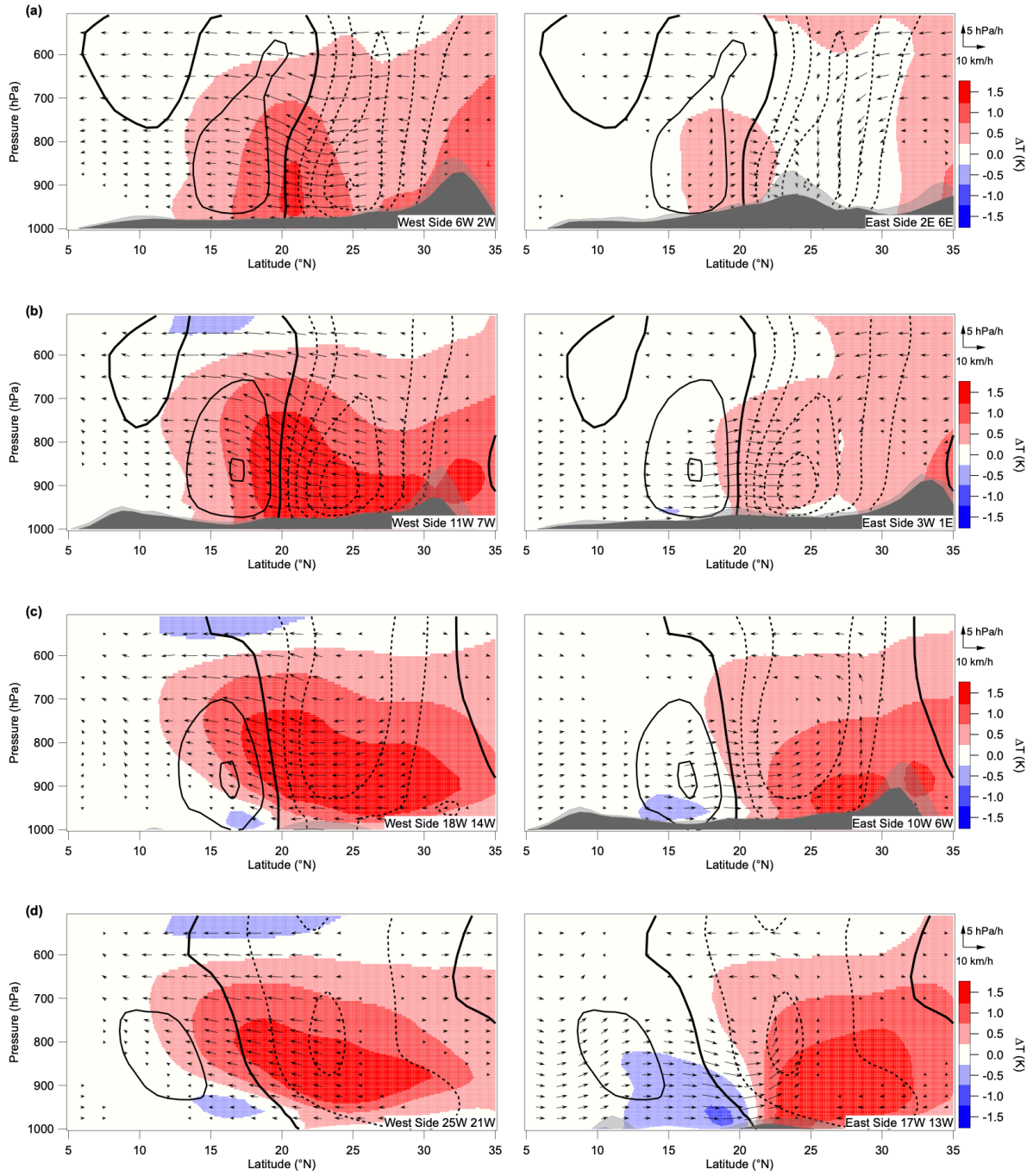

Figure 10: July and August latitudinal distribution of the anomaly of the temperature profiles (colors) and meridional and vertical wind (arrows) averaged over the west side (left) and the east side (right) of the composite vortex for (a) d_0, (b) d_0+1 day, (c) d_0+2 days, and (d) d_0+3 days. are superposed. The longitudes defining the west and east sides are indicated on the lower right corner of each panel. The corresponding zonal wind anomalies (contours, $\Delta u = \pm 1$ ms^{-1} starting from 0 with bold contour) is averaged for the central part of the vortex located between the west and east sides. The average (dark grey) and the maximum (light grey) orography for the west and the east side of the vortex are also displayed.

northwest of the Hoggar. The associated perturbation of northeasterly and subsiding winds up to 500 hPa is consistent with a reinforcement of the Libyan high circulation associated with the "Gibraltar high" anomaly. A warming of more than 1K extends roughly between the

surface and 700 hPa on the west side of the vortex (Fig.10a) and certainly contributes to the deepening of the vortex depression for the following day.

At d_0+1 day around 5°W (Fig.10b), the vortex is more axisymmetric and stronger with larger warming on the west side for air rising over the monsoon flow. On the east side, a colder and moister southerly wind perturbation penetrates further north. At d_0+2 days around 12°W (Fig.10c), the vortex is shifted upward with maximum easterlies around 800 hPa on the north side. On the west side, the warming is maximal around 800 hPa at 15°N and located above a cold anomaly at the surface. Both the northerly wind uplift on the west side and the southerly wind uplift on the east side (Fig.9c and 10c) participate in the vortex uplift. This tendency is reinforced at d_0+3 days (Fig.10d) with wind perturbations maximal around 800 hPa at 19°W. This vortex ascent during its travel between the Hoggar and the coast may be attributed to the lift of the Saharan air above the monsoon flow on its west side and to the lift possibly related to orography on its east side after d_0+2 days. This is consistent with the lifting process analyzed by Drame et al. (2011) for a Saharan Air Layer (SAL) episode that occurred in July 2010 in association with a westward moving thermal low that is indeed one of the 166 Hoggar vortices considered here.

An exhaustive computation of the energy budget of the vortices is outside the scope of this study. However, two important kinetic energy conversion parameters may be estimated on the basis of the composite perturbations in order to estimate the consistency with the energy budget of AEW-N at low-level. Previous results on AEWs (e.g., Norquist et al. 1977, Lau and Lau 1992, Diedhiou et al. 2002, Alaka and Maloney 2014, Hamilton et al. 2020, White et al. 2021) found large positive values of the baroclinic overturning term and of the barotropic conversion term at low levels around 20°N and west of the Hoggar. These terms represent respectively the conversion of eddy available potential energy to eddy kinetic energy (C_{pk}) and the transfer of mean to eddy kinetic energy (C_k) and are defined as:

$$C_{pk} = -\frac{R}{P}\overline{\omega' T'} \quad ; \quad C_k = -\overline{[\boldsymbol{V}'_H . (\boldsymbol{V}' . \nabla)\overline{\boldsymbol{V}_H}]}$$

where **V** is the three-dimensional wind, V_H is horizontal wind (m s^{-1}), ω is pressure velocity (Pa s^{-1}), T is air temperature (K). The prime is used to represents composite anomalies (i.e., eddy perturbations) and the overbar represents an average between d_0-4 days and d_0+3 days. As expected, the warm northerly wind anomaly rising on the west side of the vortex and the cold southerly wind anomaly subsiding on the east side of the vortex (Fig.9c and 9d) give a

large positive C_{pk} at low-levels around 20°N between the Hoggar and the coast (Fig.11a) in agreement with previous results on AEW-N. There is also large C_{pk} south of the Atlas Mountains, due to rising warm air in the north side of the vortex (Fig.10c and 10d). However, the nearly null C_{pk} near the Hoggar shows that baroclinic energy conversion plays no role in vortex genesis. Figure 11b shows large positive barotropic conversion C_k due to the large average cyclonic shear and the asymmetry of the vortex dominated by the northeasterly winds. This suggests that the kinetic energy of the vortex during its genesis and for its progression comes mainly from the mean northeasterly winds accelerated by the "Gibraltar High". This large C_k at low-level is also in agreement in location and amplitude with previous studies on AEW-N.

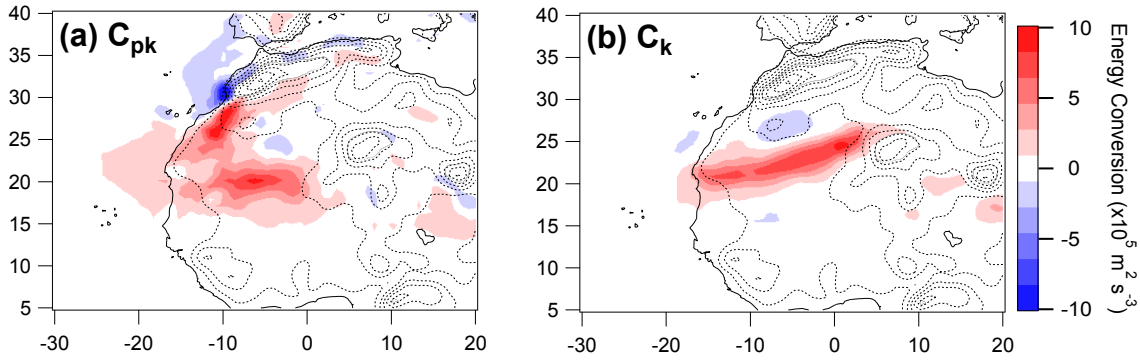

Figure 11: (a) baroclinic overturning (C_{pk}) and (b) barotropic energy conversion (C_k) between d_0-4 days and d_0+3 days at 900hPa.

6. Summary and discussion

Most of the low-level synoptic vortices formed over West Africa and propagating to the Atlantic Ocean (i.e., Atlantic vortices) on the AEW-N track are initiated downwind of the Hoggar Mountains in July and August. The main specificity in the local circulation for these months compared to June and September is the reinforcement of the low-level easterly winds over the Hoggar and the vertical expansion of subsiding easterly winds up to 400 hPa. This vertical expansion favors the development of a low-level easterly jet that may be hampered in June and September due to westerly winds above 800 hPa. The reinforcement and the larger vertical expansion of these easterlies in July and August are associated with the northward migration of the SHL. At the synoptic time-scales, the vortex initiation is associated with an additional strengthening of these easterlies over the Hoggar. This extra strengthening is associated with a high-pressure anomaly that develops first at mid-level around the Strait of Gibraltar three days before Hoggar vortex initiations and then extends downward. Locally,

this "Gibraltar high" anomaly corresponds to an amplification of the Libyan anticyclone which is also a characteristic of July. Hoggar vortex initiations are also statistically associated with a depression coming from the east and located at around 30°E at d_0-3 days. This "easterly low" appears first at low-level and then strengthens and extends up to 500 hPa before Hoggar vortex initiation. The precise origin of the "Gibraltar high" anomaly is probably multifactorial and deserves further studies. It could be related in particular to the SHL intraseasonal variability mode studied by Chauvin et al. (2010). This mode is linked to polar and subtropical jet fluctuations over the North Atlantic with a characteristic time scale of about 15 days and has some resemblance with the persistent mid-level wind anomaly around the "Gibraltar high".

The composite analysis thus objectively reveals that Hoggar vortices are statistically associated with the evolution of two features, the "Gibraltar high" and an "easterly low", both of which appear more than three days before vortex initiation. However, this composite initiation scenario being statistical, Hoggar vortices are certainly developing with various combination of these two features that are basically disconnected. The "Gibraltar high" indeed evolves over a much longer time-scale, as shown by its persistence in Figures 7 and 9, compared to the more frequent and faster "easterly low". The wave pattern evident in Figure 7, especially in Figure 7c at d_0-2 days, suggests that the "easterly low" statistically corresponds to the eastern trough of an initially weak easterly wave. The "Gibraltar high" clearly extends southward and downward as the ridge of this wave crosses the Greenwich meridian. Statistically, the Hoggar vortex initiation correspond therefore to an intensification of this easterly wave by the formation of an orographic vortex while transient northeasterly winds blow over the Hoggar between this reinforced ridge and the eastern trough. As suggested in figure 11b, the source of intensification of this vortex could be mostly kinetic energy transfer from the persistent northeasterly flow provided by the southward and downward extension of the "Gibraltar high" perturbation.

An important point is that both features lead to reinforced northeasterly wind over the Hoggar before vortex initiation southwest of the Hoggar about 1000 km east of the center of the "easterly low". The flow pattern around the Hoggar near initiation time shows some analogy with the transient period in the simulations analyzed in MZa, MZb and Zehnder (1991) which leads to a so-called starting vortex attributed to column stretching as the air initially at the top of the mountain is forced downstream. For the observed Hoggar vortices,

557 the transient character could result from the rapid intensification of the easterly flow due to
558 the Gibraltar high development. One day before vortex initiation, the reinforcement of the
559 northeasterly flow northwest of the Hoggar leads to a cyclonic vorticity anomaly in the lee of
560 the mountain. The vortex then amplifies asymmetrically with a reinforcement of the wind and
561 of the cyclonic vorticity north of its center and becomes afterward more symmetric with an
562 amplification of the monsoon flow on its south side. The present analysis is concerned mostly
563 with the origin of the vortices and their impact on the AEW-N amplitude. As might be
564 expected, the vortex characteristics after their initiation resemble those of the AEW-N
565 reported in the literature since the pioneering work of Carlson (1969) and Burpee (1972).
566 Among the 166 Hoggar vortices, there are about 20% which are following a previous one and
567 forming therefore a sort of wave packet of larger amplitude. In the composite Hoggar vortices
568 shown in Figures 7 and 9, the trough which forms statistically near 30°E at d_0-3d is located at
569 approximately 35° east of the previous vortex (Fig.7c) and takes about 4-5 days to reach the
570 position of this previous vortex, which is within the typically observed wavelength and period
571 of AEWs. The maintenance of this vortex up to the coast may be attributed to low-level
572 barotropic and baroclinic energy conversions resulting mostly from the strong cyclonic shear
573 between the northeasterlies and the monsoon flow, in agreement with previous studies on
574 AEW-N.

575 The two paths of the AEWs are well known, but they are often considered as the
576 expression of the same phenomenon having its origin in the instability of the AEJ. For
577 example, in Kiladis et al. (2006) and Hall et al. (2006), differences in the nature of AEWs are
578 mostly attributed to differences in the basic-state AEJ depending in particular on the season.
579 Hall et al. (2006) also highlight the fact that the modal growth in a dry model is not sufficient
580 to account for the presence of AEWs and that a triggering of the wave is necessary. This
581 triggering is generally attributed to convective warming in the heart or at the root of the AEJ
582 (see e.g., Thorncroft et al. 2008). It is interesting to note that Thorncroft et al (2008) found
583 that the maximum triggering efficiency is obtained for a shallow convective warming at
584 20°N-15°E, that is the statistical position of approaching trough one day before initiation
585 (Fig.7c). While the model used in Thorncroft et al. (2008) has no orography, it still has the
586 temperature structure of the SHL and the associated large-scale barotropic and baroclinic
587 instabilities. As shown in previous studies (see e.g., Grogan et al. 2016, Nathan et al. 2017),
588 this triggering could also be due to the warming resulting from the radiative forcing of
589 Saharan mineral dust. The role of mid-latitudes in triggering AEWs has also been highlighted

in Leroux et al. (2011) who showed using an idealized model that AEW packets can be associated with a slow eastward moving high pressure over the North Atlantic that presents similitudes with the “Gibraltar high” and with the perturbations at the origin of the SHL variability in Chauvin et al. (2010).

The results presented above offer another possibility for the triggering or intensification of AEW-N by invoking the impact of orographic disturbances caused by enhanced easterly winds over the Hoggar. This assumption does not contradict that of White et al (2021) who attribute the marked decrease in AEW-N energy in a model where the Hoggar and Tibesti mountains have been removed to the reduction in baroclinic energy conversion due to reduced vertical wind shear. This weaker vertical shear results from enhanced low-level easterlies to the west of the Hoggar and to a weaker AEJ due to reduced meridional surface temperature gradient (see also Hamilton et al. 2017). In fact, both processes may explain the high sensitivity of the AEW-N amplitude to the removing of the Hoggar and Tibesti orography in the White et al. (2021) sensitivity test. The “vertical shear hypothesis” considers that reinforced easterlies west of the flattened Hoggar region inhibit AEW-N, while the "orographic perturbation hypothesis” considers that reinforced easterlies over the orography is a source of intensification of AEW-N. To test more specifically the "orographic perturbation hypothesis” proposed here, additional sensitivity tests could be performed by varying the intensity and the vertical profile of the wind over the Hoggar orography, for example by imposing different latitudinal positions of the SHL.

Acknowledgments

I thank Nick Hall, François Lott, Hugo Bellenger and three reviewers for reading the manuscript and for making helpful comments and suggestions. ECMWF ERA-Interim data used in this study have been obtained from the ECMWF data server and processed on the IPSL mesocenter ESPRI facility which is supported by CNRS, UPMC, Labex L-IPSL, CNES and Ecole Polytechnique.

Data Availability Statement

ERA-Interim data used in this study are openly available at https://www.ecmwf.int/.

621

622 REFERENCES

623 Abdou, K., D. J. Parker, B. Brooks, N. Kalthoff and T. Lebel, 2010: The diurnal cycle of
624 lower boundary-layer wind in the West African monsoon, *Q. J. Roy. Meteor. Soc.*, **136**,
625 66–76.

626 Alaka, G. J., and E. D. Maloney, 2014: The intraseasonal variability of African easterly wave
627 energetics. *J. Climate*, **27**, 6559–6580.

628 Berry, G., and C. D. Thorncroft, 2005: Case study of an intense African easterly wave. *Mon.*
629 *Wea. Rev.*, **133,** 752–766.

630 Bou Karam, D., C. Flamant, P. Tulet, M. C. Todd, J. Pelon, and E. Williams, 2009: Dry
631 cyclogenesis and dust mobilization in the intertropical discontinuity of the West African
632 Monsoon: A case study, *J. Geophys. Res.*, **114**, D05115.

633 Burpee, R. W., 1972: The origin and structure of easterly waves in the lower troposphere of
634 North Africa. *J. Atmos. Sci.*, **29**, 77– 90.

635 Carlson, T. N., 1969: Synoptic histories of three African disturbances that developed into
636 Atlantic hurricanes. *Mon. Wea. Rev.*, **97,** 256–276.

637 Chauvin, F., R. Roehrig, and J.-P. Lafore, 2010: Intraseasonal variability of the Saharan heat
638 low and its link with midlatitudes. *J. Climate*, **23**, 2544–2561.

639 Chen, S.-H., and Y.-C. Liu, 2014: The relation between dry vortex merger and tropical
640 cyclone genesis over the Atlantic Ocean. *J. Geophys. Res. Atmos.*, **119**, 11 641–11 661.

641 Chen T. C., S-Y. Wang, and A. J. Clark, 2008. North Atlantic hurricanes contributed by
642 African easterly waves north and south of the African easterly jet. *J. Climate*, **21**, 6767–
643 6776.

644 Cook, K. H., 1999: Generation of the African easterly jet and its role in determining West
645 African precipitation. *J. Climate*, **12**, 1165–1184.

646 Couvreux, F., F. Guichard, O. Bock, B. Campistron, J.-P. Lafore, and J.-L. Redelsperger,
647 2010: Synoptic variability of the monsoon flux over West Africa prior to the onset. *Quart.*
648 *J. Roy. Meteor. Soc.*, **136**, 159–173

649 Cuesta J, C. Lavaysee, C. Flamant, M. Mimouni, and P. Knippertz, 2009. Northward burst of
650 the West African monsoon leading to rainfall over the Hoggar Massif, Algeria. *Q. J. R.*
651 *Meteorol. Soc.* **135**: 34–42.

652 Dee, D.P., and co-authors, 2011: The ERA-Interim reanalysis: Configuration and
653 performance of the data assimilation system. *Quart. J. Roy. Meteor. Soc.*, **137**, 553–597.

654 Diedhiou, A., Janicot, S., Viltard, A., and P. de Felice, 2002: Energetics of easterly wave
655 disturbances over West Africa and the tropical Atlantic: A climatology from 1979-95
656 NCEP/NCAR reanalyses. *Climate Dynamics*, **18**, 487–500.

657 Drame, M., G. S. Jenkins, M. Camara, and M. Robjhon, 2011: Observations and simulation
658 of a Saharan air layer event with a midtropospheric dust layer at Dakar, Senegal, 6–7 July
659 2010. *J. Geophys. Res.*, **116**, D21204.

660 Duvel, J. P., 1990: Convection over tropical Africa and Atlantic Ocean during Northern
661 summer. Part II: Modulation by easterly waves. *Mon. Wea. Rev.*, **118**, 1855-1868.

662 Duvel, J. P., 2015: Initiation and Intensification of Tropical Depressions over the Southern
663 Indian Ocean: Influence of the MJO. *Mon. Wea. Rev.*, **143**, 2170–2191.

664 Duvel, J. P., S.J. Camargo and A.H. Sobel, 2017: Role of the Convection Scheme in
665 Modeling Initiation and Intensification of Tropical Depressions over the North Atlantic.
666 *Mon. Wea. Rev.*, **145**, 1495-1509.

667 Duvel, J. P., 2021: On vortices initiated over West Africa and their impact on North Atlantic
668 tropical cyclones. *Mon. Wea. Rev.,* **149**, 585-601.

669 Fiedler, S., K. Schepanski, P. Knippertz, B. Heinold, and I. Tegen, 2014: How important are
670 atmospheric depressions and mobile cyclones for emitting mineral dust aerosol in North
671 Africa?, *Atmos. Chem. Phys.*, **14**, 8983–9000.

672 Grogan, D. F. P., Nathan, T. R., and Chen, S. H.: Effects of Saharan Dust on the Linear
673 Dynamics of African Easterly Waves, *J. Atmos. Sci.*, **73**, 891911, 2016.

674 Gu, G., R. F. Adler, G. J. Huffman, and S. Curtis, 2004: African easterly waves and their
675 association with precipitation. *J. Geophys. Res.*, **109** .D04101,
676 doi:10.1029/2003JD003967.

677 Hall, N. M. J., G. N. Kiladis, and C. D. Thorncroft, 2006: Three-dimensional structure and
678 dynamics of African easterly waves. Part II: Dynamical modes. *J. Atmos. Sci.*, *63*(9),
679 2231–2245.

680 Hamilton, H. L., Núñez Ocasio, K. M., Evans, J. L., Young, G. S., and J. D. Fuentes, 2020:
681 Topographic influence on the African Easterly Jet and African Easterly Wave energetics.
682 *J. Geophys. Res.: Atmospheres*, **125**, e2019JD032138.

683 Hodges, K., D. Chappell, G. Robinson, and G. Yang, 2000: An improved algorithm for
684 generating global window brightness temperatures from multiple satellite infrared
685 imagery. *J. Atmos. Oceanic Technol.*, **17**, 1296-1312.

686 Hopsch S. B., C.D. Thorncroft, and K. Hodges, 2007: West African storm tracks and their
687 relationship to Atlantic tropical cyclones. *J. Climate* **20**: 2468 – 2483.

688 Hopsch, S. B., C. D. Thorncroft, and K. R. Tyle, 2010: Analysis of African easterly wave
689 structures and their role in influencing tropical cyclogenesis. *Mon. Wea. Rev.*, **138**, 1399–
690 1419.

691 Huppert, H. E., and K. Bryan, 1976: Topographically generated eddies. *Deep-Sea Res.*
692 *Oceanogr. Abstr.*, **23**, 655–679

693 Kiladis, G. N., C. D. Thorncroft, and N. M. J. Hall, 2006: Three-dimensional structure and
694 dynamics of African easterly waves. Part I: Observations. *J. Atmos. Sci.*, **63**, 2212–2230.

695 Knapp, K.R., M.C. Kruk, D.H. Levinson, H.J. Diamond, and C.J. Neumann, 2010: The
696 International Best Track Archive for Climate Stewardship (IBTrACS): Unifying tropical
697 cyclone data. *Bull. Amer. Meteor. Soc.,* **91**, 363–376.

698 Lau, K.-H., and N.-C. Lau, 1992: The energetics and propagation dynamics of tropical
699 summertime synoptic-scale disturbances. *Mon. Wea. Rev.*, **120**, 2523-2539.

700 Leroux, S., N. M. Hall, and G. N. Kiladis, 2011: Intermittent African Easterly Wave Activity
701 in a Dry Atmospheric Model: Influence of the Extratropics, *J. Climate*, **24**, 5378–5396.

702 Mekonnen, A., C. D. Thorncroft, and A. R. Aiyyer, 2006: Analysis of convection and its
703 association with African easterly waves. *J. Climate*, **19**, 5405–5421.

704 Mekonnen, A., and W. B. Rossow, 2018: The interaction between deep convection and
705 easterly wave activity over Africa: Convective transitions and mechanisms. *Mon. Wea.*
706 *Rev.*, **146**, 1945–1961.

Mozer, J. B., and J. A. Zehnder, 1996a: Lee vorticity production by large-scale tropical mountain ranges. Part I: Eastern North Pacific tropical cyclogenesis. *J. Atmos. Sci.*, **53**, 521–538

Mozer, J. B., and J. A. Zehnder, 1996b: Lee vorticity production by large-scale tropical mountain ranges. Part II: A Mechanism for the Production of African Waves. *J. Atmos. Sci.*, **53**, 539–549.

Nathan, T. R., Grogan, D. F. P., and Chen, S.-H.: Subcritical Destabilization of African Easterly Waves by Saharan Mineral Dust, *J. Atmos. Sci.*, **74**, 10391055, 2017.

Norquist, D. C., E. E. Recker, and R. J. Reed, 1977: The energetics of African wave disturbances as observed during phase III of GATE. *Mon. Wea. Rev.*, **105**, 334–342.

Núñez Ocasio, K. M., J. L. Evans, and G. S. Young, 2020: A wave-relative framework analysis of AEW–MCS interactions leading to tropical cyclogenesis. *Mon. Wea. Rev.*, **148**, 4657–4671.

Parker, D., R. Burton, A. Diongue-Niang, R. Ellis, M. Felton, C. Taylor, C. Thorncroft, P. Bessemoulin, and A. Tompkins, 2005: The diurnal cycle of the west African monsoon circulation. *Q. J. R. Meteorol. Soc.,* **131**: 2839– 2860.

Pytharoulis, I., and C. D. Thorncroft, 1999: The low-level structure of African easterly waves in 1995. *Mon. Wea. Rev.*, **127**, 2266–2280.

Reed, R. J., E. Klinker, and A. Hollingsworth, 1988: The structure and characteristics of African easterly wave disturbances as determined from the ECMWF operational analysis/forecast system. *Meteor. Atmos. Phys.*, **38**, 22–33.

Russell, J. O., A. Aiyyer, J. D. White, and W. Hannah, 2017: Revisiting the connection between African easterly waves and Atlantic tropical cyclogenesis. *Geophys. Res. Lett.*, **44**, 587–595, https://doi.org/10.1002/2016GL071236.

Rydbeck, A. V., and Maloney, E. D., 2014: Energetics of East Pacific easterly waves during intraseasonal events. *Journal of Climate*, ***27*** , 7603–7621.

Sultan, B., and S. Janicot, 2003: The West African monsoon dynamics. Part II: The "preonset" and "onset" of the summer monsoon. *J. Climate*, **16 ,** 3407–3427.

Thorncroft, C. D., and D. P. Rowell, 1998: Interannual variability of African wave activity in a general circulation model. *Int. J. Climatol.,***18,** 1305–1323.

737 Thorncroft, C. D., and M. Blackburn, 1999: Maintenance of the African easterly jet. *Quart. J.*
738 *Roy. Meteor. Soc.*, **125**, 763–786.

739 Thorncroft, C. D., and K. Hodges, 2001: African easterly wave variability and its relationship
740 to Atlantic tropical cyclone activity. *J. Climate,* **14,** 1166–1179.

741 Thorncroft, C. D., N. M. J. Hall, and G. N. Kiladis, 2008: Three-dimensional structure and
742 dynamics of African easterly waves. Part III: Genesis. *J. Atmos. Sci.*, **65**, 3596–3607.

743 White, J. D., A. Aiyyer and J.O. Russell, 2021: The Impact of Orography on the African
744 Easterly Wave Stormtrack. *J. Geophys. Res.: Atmospheres*, **126**, e2020JD033749.

745 Wu, M. C., O. Reale, S. D. Schubert, M. J. Suarez, R. D. Koster, and P. J. Pegion, 2009:
746 African easterly jet: structure and maintenance. *J. Climate*, **22**, 4459–4480.

747 Zehnder, J., 1991: The interaction of planetary-scale tropical easterly waves with topography:
748 A mechanism for the initiation of tropical cyclones. *J. Atmos. Sci.*, **48 ,** 1217–1230.